Materials Research Letters

ISSN: (Print) 2166-3831 (Online) Journal homepage: https://www.tandfonline.com/loi/tmrl20

Atomic structure and mechanical response of coincident stacking faults in boron suboxide

Kolan Madhav Reddy, Pan Liu, Yidi Shen, Takeshi Goto, Qi An & M. W. Chen

To cite this article: Kolan Madhav Reddy, Pan Liu, Yidi Shen, Takeshi Goto, Qi An & M. W. Chen (2019) Atomic structure and mechanical response of coincident stacking faults in boron suboxide, Materials Research Letters, 7:2, 75-81, DOI: 10.1080/21663831.2018.1556184

To link to this article: https://doi.org/10.1080/21663831.2018.1556184

MATER. RES. LETT.
2019, VOL. 7, NO. 2, 75–81
https://doi.org/10.1080/21663831.2018.1556184

MATERIALS RESEARCH LETTERS
Taylor & Francis
Taylor & Francis Group

ORIGINAL REPORT

OPEN ACCESS Check for updates

Atomic structure and mechanical response of coincident stacking faults in boron suboxide

Kolan Madhav Reddy[a], Pan Liu[a], Yidi Shen[b], Takeshi Goto[c], Qi An[b] and M. W. Chen[a,d,e]

[a]State Key Laboratory of Metal Matrix Composites, School of Materials Science and Engineering, Shanghai Jiao Tong University, Shanghai, People's Republic of China; [b]Department of Chemical and Materials Engineering, University of Nevada Reno, Reno, NV, USA; [c]Institute for Materials Research, Tohoku University, Sendai, Japan; [d]WPI Advanced Institute for Materials Research, Tohoku University, Sendai, Japan; [e]Department of Materials Science and Engineering, Johns Hopkins University, Baltimore, MD, USA

ABSTRACT

We report the atomic structure of coincident stacking faults (SFs) in superhard boron suboxide (B_6O) by combining annular bright field scanning transmission electron microscopy and quantum mechanics (QM) simulations. Different from simple SFs, which only lead to the symmetry breaking, the coincident SF junctions in the complex B_6O result in local chemical configuration changes by forming an abnormal three-oxygen-atoms chain linking boron icosahedra, instead of the regular two-oxygen-atoms chain in a perfect B_6O crystal. QM studies demonstrate that coincident SFs lead to the decreased shear strength under pure shear and indentation conditions and are responsible to the initial failure and amorphization of B_6O.

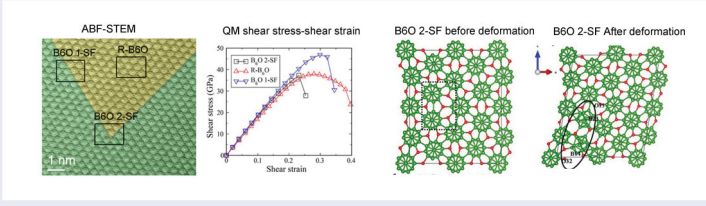

ARTICLE HISTORY
Received 12 November 2018

KEYWORDS
Boron suboxide; transmission electron microscopy; stacking fault; shear amorphization; mechanical behavior

IMPACT STATEMENT

Combining ABF-STEM and MD simulations, we demonstrated that the coincident SFs lead to the decrease of shear strength and are responsible for the initial failure and amorphization of B_6O.

Introduction

The combination of low density and super-high hardness is often desirable for structural materials and ballistic armor applications where both strength and weight are critical [1,2]. B_6O belongs to the icosahedral compounds with a rigid covalent bonding and has the promising properties of being ultra-strong ($\sim$45 GPa in hardness) and lightweight ($\sim$2.6 g/cm^3 in density) [3–5]. Technically, boron suboxide (B_6O) can be fabricated under ambient pressure without the requirements of extremely high synthesis pressures at high temperatures, unlike other superhard materials such as diamond and cubic boron nitride [2–5]. B_6O mainly exist in the form of a stoichiometric compound [2,6], which is different from boron carbide that has a wide solid solution range. The distinct properties arise from the unique atomic structure of B_6O in which two-oxygen atoms bond to the neighboring boron icosahedra (B_{12}) and do not form direct oxygen-oxygen chemical bonding in a rhombohedral unit cell [7,8]. As a result, the complex atomic configuration in B_6O has anticipated the high density of planar defects during the crystal growth [9,10].

It has been suggested that planar defects, such as twins, enhance the strength of metals and alloys, identical to that of grain boundaries (GBs) [11,12]. In particular, the interfaces of nanotwins strongly influence the mechanical and thermal properties by blocking dislocation movements [13,14]. Despite the fact that dislocations

CONTACT M. W. Chen mwchen@jhu.edu Department of Materials Science and Engineering, Johns Hopkins University, Baltimore, MD 21218, USA; Qi An qia@unr.edu Department of Chemical and Materials Engineering, University of Nevada Reno, Reno, NV 89557, USA

Supplemental data for this article can be accessed here. https://doi.org/10.1080/21663831.2018.1556184

in covalently bonded superhard materials are usually sessile at room temperature due to high lattice resistance, it has been found that nanotwins can enhance the hardness, toughness and thermal stability of diamond, BN, B_4C and B_6O [15–18]. Similar to twins and GBs, stacking faults also have a planar feature and can lead to strong interactions with dislocations for interface strengthening. For instance, Jain et al. examed an Mg alloy and showed the enhanced strength while maintaining good ductility by introducing a high density of stacking faults, which impeded dislocation slip and promoted dislocation accumulation [19]. Despite the fact that numerous stacking faults (SFs) and coincident SFs have been observed in B_6O and other superhard ceramics [9,10,15–18,20,21], their structure and influence on the mechanical properties of the superhard materials have not been explored partially due to the lack of sufficient spatial resolution to image light elements on atomic scale. In this work we investigate local atomic structure of single- and coincident SFs in B_6O crystals by means of state-of-the-art aberration-corrected annular bright field STEM (ABF-STEM) and QM simulations. The local structural and chemical variations were characterized by the experimental observations and modeled by QM simulations, which provide atomic insights into the structure and effect of SFs on mechanical properties of B_6O.

Results and discussion

Figure 1 presents an atomic resolution image of a B_6O crystal viewed in $[1\bar{1}\bar{1}]$ zone axis orientation. A representative high-resolution TEM image (Figure 1(a)) shows the high-density stacking faults (yellow lines) and twins (red lines) within a B_6O crystal. The ABF-STEM image (Supplemental Material Figure S1 and Figure 1(b)) obtained from the same B_6O crystal along the $[1\bar{1}\bar{1}]$

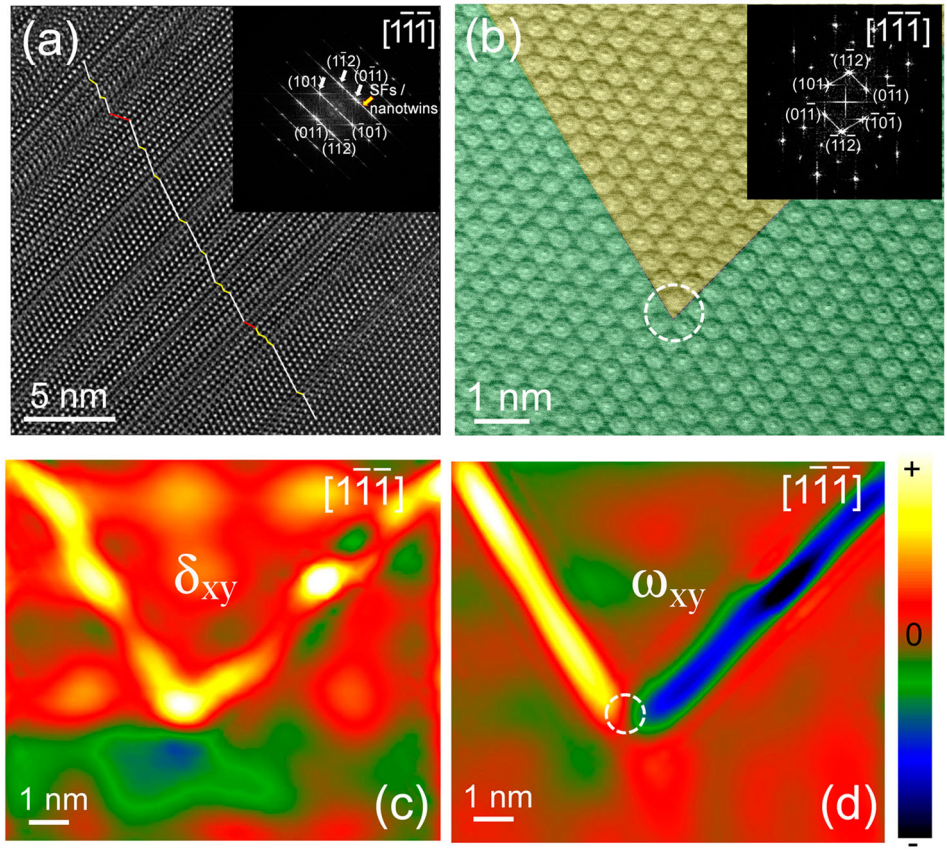

Figure 1. TEM characterization of planar defects and strain map analysis of B_6O, (a) High-resolution TEM image displaying the high-density SFs and twins in a single crystal B_6O viewed along $[1\bar{1}\bar{1}]$ direction, (b) ABF-STEM image of B_6O shows the coincident of two stacking faults (SF) within a crystal grain. The SFs interface was marked with false-coding of green and yellow colors. Inset FFT obtained from the single crystalline B_6O grain of (b) is oriented along the $[1\bar{1}\bar{1}]$ direction and the growth of SFs predominately develops along {101} planes, (c,d) Strain map of mean dilatation (δ_{xy}) and rotation (ω_{xy}) components of the ABF-STEM atomic structure obtained parallel to SF planes using peak pairs (PP) method. PP strain map and rotations was calculated using (101) and $(01\bar{1})$ structural reflections, (c) A lattice strain of δ_{xy} within a 1 nm SF region is about $\sim$3–4%. The color ranges from $\sim$5% (black) to +5% (white), (d) Lattice rotation of two SFs represented in color code by black and white, with respect to defect-free crystal (red color). The color varies from $-\pi$ to $+\pi$ using same color code. Dotted circle area in the vicinity of SFs from image (b) reveals distortion without rotation from maps (c, d).

projection clearly shows icosahedral (B_{12}) clusters in the form of atomic rings and in between a linear array of pair of oxygen atomic columns [*the experimental details are described in the Supplemental Material*].[1] In addition, the image displays coincidence of two stacking faults, their interfaces are marked with false-coding of green and yellow colors (Figure 1(b)). An inset FFT pattern in Figure 1(b) indicates that the stacking faults growth were predominately along (101) and (01$\bar{1}$) crystal planes. At proximity of the SFs intersection region, there are visible local structural distortions as represented by white circle (see Figure 1(b)). Figure 1(c,d) shows the two-dimensional maps of the mean dilatation elastic strain (δ_{xy}) and rotation (ω_{xy}) components derived from the ABF-STEM (Figure 1(a)) by using peak pairs (PP) analysis. The δ_{xy} value marginally increases to $\sim$2–4% in a $\sim$1 nm width of SFs region as compared to that of defect-free B_6O crystal. The ω_{xy} map (Figure 1(d)) elucidates the anticlockwise ($+\pi$) and clockwise ($-\pi$) structural orientation of SFs region as compared to defect-free region. By close inspection of Figure 1(c,d), the vicinity region of the SFs intersection does not undergo any structural rotation, as shown by dotted circle (Figure 1(d)).

Figure 2(a) is a low-pass filtered ABF-STEM image of Figure S1 illustrates the icosahedral atomic rings of boron (B_{12}) atoms and the positions of oxygen atoms (O–O) in a rhombohedral crystal of B_6O, which is imaged along the [1$\bar{1}\bar{1}$] direction. Although atomic columns of boron (B) in individual icosahedra are difficult to illustrate directly due to the short bond length distances along the imaging direction and curved surface of the icosahedron, two-oxygen atoms as the bright spots linking icosahedra are visible vividly. A fault of atomic plane stacking sequence is represented by B_6O-1SF and the atomic planes with two coincident stacking faults are denoted by B_6O-2SF as shown in the white box regions. The oxygen atoms in both SFs rotate to an opposite direction as compared to the defect-free B_6O crystal marked by the red dots (Figure 2(a)). The bond length of O–O atoms at the SFs is nearly identical with respect to the B_6O crystal of about 3 Å, which is consistent with predicted structure [8,9]. Figure 2(b) is the zoom-in

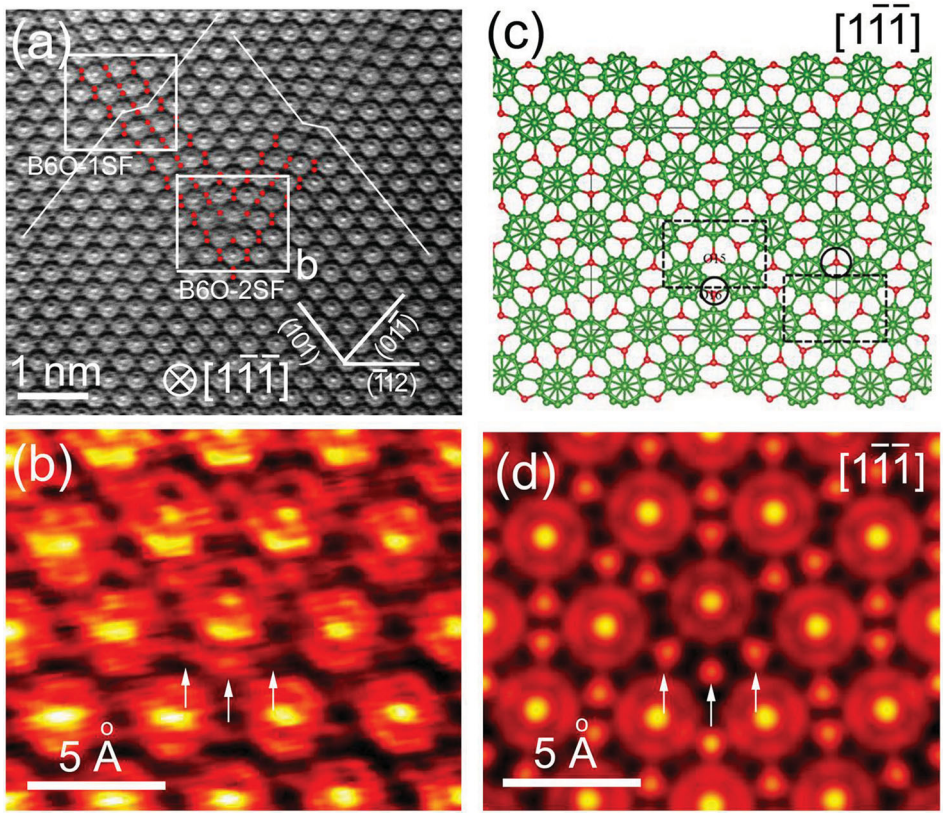

Figure 2. Atomic resolution of stacking faults viewed along [1$\bar{1}\bar{1}$] direction in a B_6O crystal, (a) Low pass filtered ABF-STEM image showing icosahedral (B_{12}) units with bound linear oxygen atoms (O–O). A fault of atomic plane stacking sequence represented by B_6O-1SF; and the coincident of two stacking faults atomic planes denoted by B_6O-2SF are shown in white box regions, (b) A magnified ABF-STEM taken from marked B_6O-2SF region shows three-oxygen atoms linked to icosahedral (white arrows) at the coincident site of two SFs, (c) Structure model constructed using QM simulations based on experimentally observed SFs atomic structure in (b). The green and red balls representing the B and O atoms, respectively. The solid line represents the supercell boundary and the dashed lines are the experimentally observed SF structure, (d) The simulated structure is well matched with ABF-STEM image of B_6O-2SF.

ABF-STEM image of Figure 2(a) at the proximity of SFs, which shows the bonding of three-oxygen atoms (O–O–O) to icosahedral as marked by red arrowheads. To examine the experimentally observed SF structure (Figure 2(a,b)), we constructed the atomic structure in which two SFs are presented with periodic boundary conditions as shown in the dashed line regions in Figure 2(c). This structure consists of 16 B_{12} icosahedra and 16 O···O chains in the supercell structure. The PBE optimized supercell structure has the lattice parameters of $a = 23.597$ Å, $b = 5.015$ Å, $c = 19.998$ Å, $\alpha = 90$, $\beta = 90$, $\gamma = 44.261$. On the basis of the QM model, we simulated the ABF-STEM image of the SFs (Figure 2(d)). The excellent consistency between the experimental and simulated ABF-STEM images justifies the reliability of the QM model. It is interesting to notice that the O–O atom chain in the SF region (along the '*a*' axis) is separated by the icosahedral B-B bond, leading to an isolated O atom (O16 in Figure 2(c)) among three icosahedra, as shown in the oval in Figure 2(c). The bond distances of this O16 atom with three nearby B atoms are only 1.443, 1.434 and 1.435 Å, which are shorter than the normal B–O bond distance in perfect B_6O (1.496 Å). However, the bond distances of O15 with three nearest B atoms increase to 1.596, 1.597 and 1.581 Å. Apparently, the local strains at the SFs (Figure 1) are associated with the structural distortions.

The SF structure leads to the energy increase of 4.49 eV per SF structure. The absolute and relative free energies of the B_6O-2SF structure were calculated and compared with those of SF-1 and R-B_6O (Table 1).

To understand how the SF structure affects the mechanical properties of B_6O, we first applied pure shear deformation along (001)[100] slip system and compared with the perfect rhombohedral B_6O [*the computational details are described in the Supplemental Material*] (see Note 1). It is worth to notice that the SF structure in simulations is orthorhombic. The slip system is perpendicular to the SF structure and gives rise to a larger shear strain within the SF region. The plot of shear stress vs shear strain is displayed in Figure 3(a). The ideal shear strength of the SF structure is 34.8 GPa at 0.209 strain, which is 3.1 GPa smaller than that of perfect B_6O (37.9 GPa) shearing along $(101)[1\bar{1}\bar{1}]$ the slip system [20]. The SF structure is also sheared along the interface and much larger shear strength (44.8 GPa) was found, indicating that shear parallel to the interface is not favorable. The details can be found in the Supplemental Material (Figure S2). Therefore, the present of SFs lower the shear strength and weaken the B_6O crystal. It is worth noticing that nanotwins can strengthen materials such as metals and c-BN [12,16]. Here in SF-2 structure, the bond distances of O15 with three nearest B atoms increase by at least 7% compared to the normal B–O bond distance. This leads to the weakening of icosahedra around SF-2 structure, lower the critical shear strength for failure. Figure 3(b–d) displays the deformation process of SF structure subjected to shearing along the (001)[100] slip system. The intact structure is displayed in Figure 3(b). As the system is sheared to 0.231 strain (corresponding to a maximum stress of 37.3 GPa) the B23-O15 bond in the SF structure is stretched from 1.596 to 1.840 Å, as shown in Figure 3(c). As the system is sheared continuously to 0.254 strain, the B23-O15 bond breaks with the B23···O15 distance increasing to 3.384 Å. Meanwhile, the icosahedron containing B23 atom is deconstructed, as shown in Figure 3(d). This leads to that the structure fails and the shear stress drops to 27.8 GPa. It is worth noticing that one icosahedron in the neighboring SF region is disintegrated because of the similar bond broken process of B14-O32, as shown in the oval in Figure 3(d). Thus, the SF structure failure initiates from the weak SF region by breaking the icosahedron-chain B–O bonds.

We also examined the failure mechanism of B_6O-1 SF, as shown in Figure S3. As the shear strain increases to 0.299 which corresponds to the maximum shear stress of 46.9 GPa, the inter-icosahedral B-B bond at SF layer (e.g. B72-B76) is stretched from 1.70 to 2.60 Å, but it is not breaking yet. As the shear strain continuously increases to 0.322, the inter-icosahedral B-B bond is stretched to 3.23 Å and breaks, leading to the decrease of shear stress from 46.9 to 45.90 GPa. As the shear strain further increases to 0.345, the O-B bonds (e.g. O16-B80) break and O16-B76 bond forms. Then the icosahedra rotate without breaking the icosahedra, leading to the shear stress significantly drops. The B_6O-1 SF increases the strength compare to the perfect B_6O because the slip system along the SF is different compared to perfect B_6O [21]. In perfect B_6O, the most plausible slip system is $(101)[1\bar{1}\bar{1}]$, while the shear along SF plane is along $[001]<100>$ rhombohedral slip system.

Indentation experiments are used to estimate the hardness of materials. To mimic the stress conditions under indentation experiments [29], we applied biaxial shear strains on the SF structure and compared to that of perfect B_6O. The shear stress versus shear strain curves of the SF structure and perfect crystals under biaxial shear are displayed in Figure 4(a). The critical shear stress of SF

Table 1. Absolute energies of B_6O for single crystal B_6O, B_6O-1 SF and B_6O-2 SF.

Structure	Single crystal B_6O	B_6O-1SF	B_6O-2SF
Energies (eV/ B_6O unit)	−50.13	−49.98	−49.90
Relative energy (meV/ B_6O unit)	0	0.15	0.23

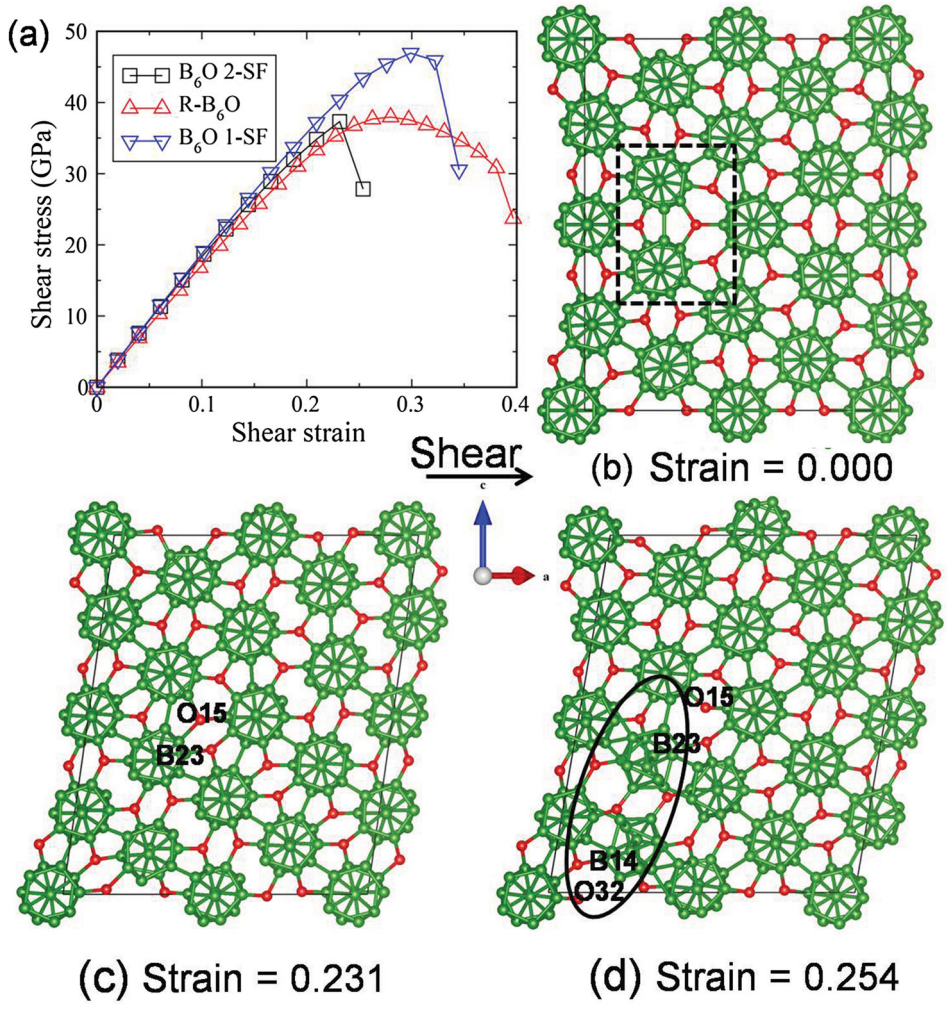

Figure 3. (a) The shear stress–shear strain relationship of B_6O-2 SF structure under pure shear were compared to B_6O-1 SF and single crystal B_6O, Snapshots of B_6O-2 SF (b) Intact structure, (c) Structure at 0.231 strain corresponding to the maximum shear stress of 34.8 GPa, (d) Failure structure at 0.254 strain. The deconstructed icosahedra are in the oval.

structure along (001)[100] slip system is only 24.9 GPa, while it is 37.2 GPa for the perfect B_6O shearing along (101)[$1\bar{1}\bar{1}$] slip system which has lowest shear strength in perfect B_6O [20]. Thus, the critical shear stress is significantly decreased as SF structure presents under indentation conditions. The deformation process for SF structure under indentation conditions is displayed in Figure 4(b–f). As the shear strain increases from the intact structure (Figure 4(b)) to 0.144, corresponding to the shear stress of 24.8 GPa, the B23-O15 bond is stretched from 1.596 to 1.639 Å (Figure 4(c)). The bond length increase is less than that of pure shear deformation because of the biaxial shear stress conditions. Then, the B23-O15 bond is broken as it increases to 2.665 Å at 0.166 strain (Figure 4(d)). The corresponding shear stress (the maximum shear stress) is just 24.9 GPa. In comparison with pure shear, the maximum shear stress for the bond breaking of B23-O15 slightly increases and the icosahedral clusters are not deconstructed. As the shear strain increases to 0.187, the shear stress decreases to 24.7 GPa. Correspondingly, the B108 atom is stretched out from the icosahedron near the SF structure (Figure 4(e)) and two icosahedra are deconstructed. As the shear strain continuously increases to 0.209, the shear deformation deconstructs the icosahedra with missing boron atoms in the previous step (Figure 4(f)). In addition, two additional icosahedra in the other SF region are deconstructed, as shown in Figure 4(f). This leads to the failure of SF structure by amorphization, accompanying with a significant drop of shear stress to 15.0 GPa.

The failure mechanism of B_6O-1 SF under biaxial shear deformation is shown in Figure S4. As the shear strain increases to 0.276 corresponding to the maximum shear stress of 41.5 GPa, the icosahedral B-B bond at both side of SF (e.g. B8-B16) is stretched from 1.79 to 2.14 Å, but it is not breaking yet. As the shear strain continuously increases to 0.299, the B8-B16 bond is stretched to 2.14 Å and breaks, leading to a slight decrease of shear

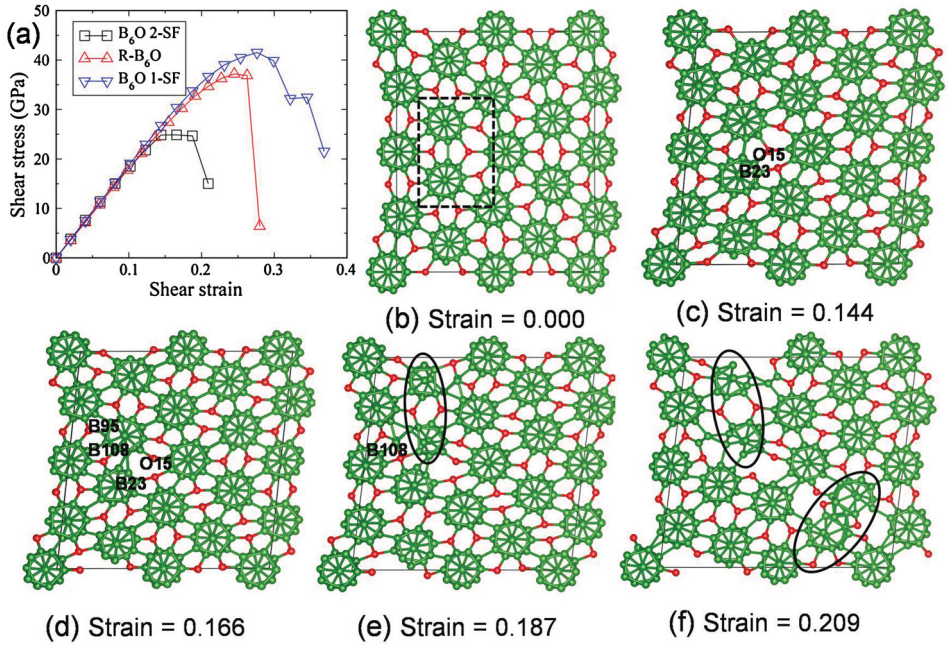

Figure 4. (a) The shear stress–shear strain relationship of B_6O-2 SF structure under biaxial shear were compared with B_6O-1 SF and single crystal B_6O, B_6O-2 SF (b) Intact structure, (c) Structure at 0.144 strain corresponding to 24.8 GPa shear stress, (d) Structure at 0.144 strain corresponding the maximum shear stress of 24.9 GPa, (e) Structure at 0.187 strain before failure, (f) Failure structure at 0.209 strain. The deconstructed icosahedra are in the oval.

stress from 41.5 to 39.9 GPa. As the shear strain further increases to 0.322, these icosahedra at both sides of SF are disintegrated, leading to a decrease of the shear stress to 32.2 GPa. At 0.369 shear strain, B–O bonds in the SF break, leading to the shear stress drastically decrease to 21.5 GPa and failure.

Conclusions

In this study, we have characterized the atomic structure and mechanical response of single- and coincident SFs using ABF-STEM and QM simulations. The ABF-STEM images reveal the coincident SFs junctions linked with three-oxygen atoms (O–O–O), instead commonly observed O–O chains bonded to icosahedral B_{12} clusters in single SFs and perfect B_6O structure. The coincident SFs possess obvious local distortions with 3–4% dilatation strains, which lead to the increase of free energy as compared to single SFs and perfect B_6O. QM simulations indicate that failure under shear initiates from the distorted SF region by breaking the icosahedral-chain B–O bonds at a relatively lower shear stress. The critical shear stress of coincident SFs under the pure shear stress and indentation conditions along (001)[100] slip systems are about 9% and 33% lower than the shear strength of perfect B_6O. The weakening results from the preferential deformation and structure damage by amorphization at the defect sites. These results underscore the importance of crystal defects in the failure and damage of complex materials with ultra-high strength.

Note

1. See Supplemental Material, which includes Refs. [22–28], for (i) experimental details, (ii) computational details, (iii) Figure S1. Atomic resolution ABF-STEM image of SFs B_6O, The unsmoothed (Raw) ABF STEM image and FFT patterns clearly demonstrate single SFs (b and c) and coincident SF (d) at intersection region in a single crystal B_6O (a and e). (iv) Figure S2. The shear deformation along the SF plane in the coincident SFs structure, (a) Shear model, (b) Shear stress vs shear strain relationship showing a higher strength than slip system in Figure 3. (v). Figure S3. The pure shear deformation along the SF plane in the 1-SF structure: (a) Intact structure; (b) structure at 0.299 shear strain corresponding to the maximum shear stress; (c) at 0.322 shear strain just passing the critical shear stress; (d) failure structure at 0.345 shear strain. (vi) Figure S4. The biaxial shear deformation along the SF plane in the 1-SF structure: (a) Intact structure; (b) structure at 0.276 shear strain corresponding to the maximum shear stress; (c) structure at 0.299 shear strain; (d) failure structure at 0.322 shear strain; (e) failure structure at 0.369 shear strain.

Acknowledgments

The authors would like to thank Dr Takeshi Fujita and Dr Akihiko Hirata at the WPI-AIMR, Japan for assistance in strain analysis and image processing.

Disclosure statement

No potential conflict of interest was reported by the authors.

Funding

This work was sponsored by the 973 program of Ministry of Science and Technology of the People Republic of China [grant number 2015CB856800], National Natural Science Foundation of China [grant numbers 11327902, 51271113, 11704245 and 51850410501]; and the fusion research program of 'World Premier International Research Center (WPI) Initiative' by JSPS, Japan. M.C. was sponsored by Whiting School of Engineering, Johns Hopkins University. Q.A. supported by U.S. National Science Foundation [CMMI-1727428] and U.S. Nuclear Regulatory Commission [NRC-HQ-84-15-G-0028].

References

[1] Kaner RB, Gilman JJ, Tolbert SH. Designing superhard materials. Science 2005;308:1268–1269.
[2] Domnich V, Reynaud S, Haber RA, et al. Boron carbide: structure, properties, and stability under stress. J Am Ceram Soc. 2011;94:3605–3628.
[3] McMillan PF. New materials from high pressure experiments. Nat Mater. 2002;1:19–25.
[4] Herrmann, Sigalas MI, Thiele M, et al. Boron suboxide ultrahard materials. Int J Refract Metals Hard Mater. 2013;39:53–60.
[5] He D, Zhao Y, Daemen L, et al. Boron suboxide: As hard as cubic boron nitride. Appl Phys Lett. 2002;81:643–645.
[6] Solozhenko VL, Kurakevych OO, Turkevich VZ, et al. Phase diagram of the B-B_2O_3 system at 5 GPa: experimental and theoretical studies. J Phys Chem B 2008;112:6683–6687.
[7] Reddy KM, Liu P, Hirata A, et al. Atomic structure of amorphous shear bands in boron carbide. Nat Commun. 2013;4,2483.
[8] Kobayashi M, Higashi I, Brodhag C, et al. Structure of B_6O boron suboxide by rietveld refinement. J Mater Sci. 1993;28:2129–2134.
[9] Hubert H, Devourd B, Garvie LAJ, et al. Icosahedral packing of B12 icosahedra in boron suboxide (B_6O). Nature 1998;391:376–378.
[10] Reddy KM, Hirata A, Liu P, et al. Shear amorphization of boron suboxide. Scripta Mater. 2014;76:9–12.
[11] Lu L, Shen Y, Chen X, et al. Ultrahigh strength and high electric conductivity in copper. Science 2004;304:422–426.
[12] Lu K, Lu L, Suresh S. Strengthening materials by engineering coherent internal boundaries at the nanoscale. Science 2009;324:349–352.
[13] Li XY, Wei Y, Lu L, et al. Dislocation nucleation governed softening and maximum strength in nano-twinned metals. Nature 2010;464:877–880.
[14] Sim GD, Krogstad JA, Reddy KM, et al. Nanotwinned metal MEMS films with unprecedented strength and ductility. Sci Adv. 2017;3:e1700685.
[15] Tian Y, Xu B, Yu D, et al. Ultrahard nanotwinned cubic boron nitride. Nature 2013;493:385–388.
[16] Huang Q, Yu D, Xu B, et al. Nanotwinned diamond with unprecedented hardness and stability. Nature 2014;510:250–253.
[17] An Q, Goddard III WA, Xie KY, et al. Superstrength through nanotwinning. Nano Lett. 2016;16:7573–7579.
[18] Kunka C, An Q, Rudawski N, et al. Nanotwinning and amorphization of boron suboxide. Acta Mater. 2018;147:195–202.
[19] Jian WW, Cheng GM, Xu WZ, et al. Ultrastrong Mg alloy via Nano-spaced stack faults. Mater Res Lett. 2013;1:61–66.
[20] An Q, Reddy KM, Qian J, et al. Nucleation of amorphous shear bands at nanotwins in boron suboxide. Nat Commun. 2016;7:11001.
[21] An Q, Reddy KM, Dong HF, et al. Nanotwinned boron suboxide (B_6O): New ground state of B_6O. Nano Lett. 2016;16:4236–4242.
[22] Akashi T, Itoh T, Gunjishima I, et al. Thermoelectric properties of hot pressed boron suboxide (B_6O). Mater Trans. 2002;43:1719–1723.
[23] Galindo PL, Kret S, Sanchez AM, et al. The peak pair algorithm for strain mapping from HRTEM images. Ultramicroscopy 2007;107:1186–1193.
[24] Kresse G, Hafner J. Ab initio molecular dynamics for liquid metals. Phys Rev B 1993;47:558–561.
[25] Kresse G, Furthmuller J. Efficiency of ab-initio total energy calculations for metals and semiconductors using a plane-wave basis set. J Comput Mater Sci. 1996;6:15–50.
[26] Kresse G, Furthmüller J. Efficient iterative schemes for ab initio total-energy calculations using a plane-wave basis set. J Phys Rev B 1999;16:11169–11186.
[27] Kresse G, Joubert D. From ultrasoft pseudopotentials to the projector augmented-wave method. Phys Rev B 1999;59:1758.
[28] Roundy D, Krenn CR, Cohen ML, et al. Ideal shear strengths of fcc aluminum and copper. Phys Rev Lett. 1999;82:2713–2716.
[29] Li B, Sun H, Chen CF, Large indentation strain-stiffening in nanotwinned cubic boron nitride. Nat Commun. 2014;5:4965.